

Liu, Su, Reichard, Yin: Calibration-based phase-shifting projected fringe profilometry for accurate absolute 3D surface profile measurement

Thursday, February 11, 2021 2:08 PM



1-s2.0-S003
04018020...



Available online at www.sciencedirect.com

SCIENCE @ DIRECT®

Optics Communications 216 (2003) 65–80

OPTICS
COMMUNICATIONS

www.elsevier.com/locate/optcom

Calibration-based phase-shifting projected fringe profilometry for accurate absolute 3D surface profile measurement

Hongyu Liu^a, Wei-Hung Su^a, Karl Reichard^b, Shizhuo Yin^{a,*}

^a Department of Electrical Engineering, The Pennsylvania State University, University Park, PA 16802, USA

^b Applied Research Laboratory, The Pennsylvania State University, University Park, PA 16804, USA

Received 19 August 2002; received in revised form 11 November 2002; accepted 25 November 2002

Abstract

In this paper, an accurate calibration-based phase-shifting measurement technique for measuring the absolute 3D surface profiles is presented, in which the system distortions for each detection location are calibrated individually. Thus, this approach offers higher accuracy than that of conventional global system model-based calibration technique. By comparing the experimental results from this technique with the data from Zeiss Universal Precision Measuring Center (Model UPMC 550), it is found that the absolute measurement accuracy for a bowl size object (about 160 mm in diameter and 40 mm in depth) is about 5 μm . This experimental result proves that, indeed, this calibration-based phase-shifting measurement technique has a good enough accuracy for precise engineering surface (such as gear gauge surface) measurement.
© 2002 Elsevier Science B.V. All rights reserved.

Keywords: Projected fringe profilometry; Phase-shifting technique; 3D surface profile measurement

1. Introduction

Phase-shifting projected fringe profilometry (PSPFP) is a powerful tool for the 3D surface profile inspection of rough engineering surfaces [1–7]. With a phase-shifting detection scheme, accuracy better than one part in ten thousands of the field of view can be achieved even with excessive image noise. In many profiling applications, PSPFP is notable for its non-contact nature, full-field measurement capability, high profile sampling density, and low environmental vulnerability.

Non-telecentric PSPFP systems have been widespread in use because of their capability of handling a relatively large field of view [8]. However, systematic methodologies have not been developed for accurately characterizing the nonlinear phase-to-depth relation in this type of systems. Uncertainties in phase-to-depth conversion can be translated directly to the final measurement error and thus become a limiting factor in

*Corresponding author. Fax: +1-814-865-7065.

E-mail address: sxy105@psu.edu (S. Yin).

many cases [9]. Another scenario occurs when the lateral geometry of test objects is of interest. In the prime form of PSPFP, only the depth position of a sampled surface point can be accurately determined, but not its transversal position [1,8]. In many previously reported works, image lateral geometry has often been used to approximate object lateral geometry. Such an approach fails when the imaging system sustains considerable amount of distortion, which is unfortunately true for most off-the-shelf cameras. Without solving these problems, the use of PSPFP is limited to simple pass-and-fail types of inspections.

The causes of the above problems may be due to the fact that PSPFP was not originally developed for accurate, absolute shape measurements. Some approaches combining photogrammetry and PSPFP techniques have been reported recently in an attempt to solve these problems [10–14]. These techniques are mainly based on the theoretical framework of photogrammetry and require at least two cameras or two projectors. Their applicability may be restricted in applications where the measured regions have to be visible to both the cameras and the projectors simultaneously. Two-camera or two-projector configurations are also not preferred when system compactness becomes a critical design criterion. Of course, one can use a reduced triangulation angle to alleviate both problems. But this can only be accomplished at the cost of decreased measurement sensitivity.

In this paper, we propose an accurate calibration-based phase-shifting measurement scheme for finding the absolute shape of objects. It employs the conventional one-camera and one-projector configuration, which enables higher flexibility in measurements and more compactness in hardware implementation. In a direct analogy to the two-plane calibration scheme, this technique characterizes system distortions individually for each detection location. Such an approach effectively accounts for local distortion effects and therefore is potentially more accurate than those depending on a global system model. The estimation of system parameters requires only a linear optimization in which numerically stable solutions are guaranteed. Finally, the system model underlying the calibration process encompasses the case in which the detection plane is not perpendicular to the optical axis of the imaging lens. This makes the current technique especially adaptable to some specially configured measurement systems such as precision gear-gauging and large scale profile inspections.

2. Measurement principles

2.1. Basic definitions and assumptions

Fig. 1 shows the coordinate systems in a typical non-telecentric PSPFP measurement system. World coordinate system XYZ is a fixed reference system for representing the shape of tested objects. Detection plane coordinate system RC is defined in the CCD detection plane with axes R and C parallel to the row and the column directions of the sensor array, respectively. The origin of the RC coordinate system is chosen as the center of the upper-left pixel. The origin of the camera coordinate system, UVW , is the nodal point of the imaging lens. Axis W coincides with the optical axis of the imaging lens. The origin of the grating coordinate system is a specially marked point in which the absolute phase is specified as zero. The grating lies in the X_gY_g plane with fringes normal to axis X_g . The definition of the projector coordinate system is self-explanatory because of its similarity to the camera coordinate system.

A point can be mapped from one reference system to another by applying a rotation matrix and a translation vector. For example, a point (r, c) in the detection-plane coordinates is represented by (u, v, w) in the camera reference system, the two sets of coordinates are related by

$$\begin{bmatrix} u \\ v \\ w \end{bmatrix} = \begin{bmatrix} r_{11}^{DC} & r_{12}^{DC} & r_{13}^{DC} \\ r_{21}^{DC} & r_{22}^{DC} & r_{23}^{DC} \\ r_{31}^{DC} & r_{32}^{DC} & r_{33}^{DC} \end{bmatrix} \begin{bmatrix} r \\ c \\ 0 \end{bmatrix} + \begin{bmatrix} t_x^{DC} \\ t_y^{DC} \\ t_z^{DC} \end{bmatrix}. \quad (1)$$

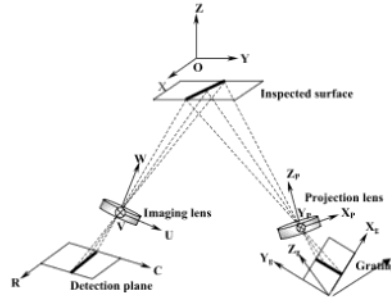


Fig. 1. Coordinate systems in a non-telecentric PSPFP measurement system.

Here, symbols 'D' and 'C' in the superscripts represent the detection-plane and the camera coordinate systems, respectively. The order of these symbols indicates the direction of the coordinate transformation. This convention also applies to the future discussion.

In the above definitions, the CCD detection plane is not necessarily perpendicular to the optical axis of the imaging lens. Neither is the grating plane with respect to the optical axis of the projection lens. When a close object is obliquely observed, the grating plane and the detection plane are often oriented roughly conjugate to the object surface. This is especially necessary when the depth of field of the optical system becomes limited compared to the depth of the object.

Except for geometric distortions, assume that the other aberrations of the imaging and the projection systems are carefully corrected in advance. In practice, such an assumption is usually enforced by stopping down the respective lenses. By doing so, the aberrations proportional to the high-order powers of aperture size can be suppressed significantly. Image points are defined as the point of intersection with the detection plane of principle rays. To compensate the reduced illumination when a small aperture is used, the exposure time on the CCD detector can be increased.

As in other phase-shifting position measurement systems, a phase value sampled at an object point is assumed equal to that sampled at its image point. This assumption applies when sinusoidal fringes are well resolved by the optical system and the point-spread function of the system is symmetric (coma-free).

2.2. Calibration-based phase-shifting profile measurement

Consider an arbitrary surface point (x, y, z) in the world coordinate system in which the sampled absolute phase is φ . According to the assumption given in the previous section, same absolute phase will be obtained at its image point (r, c) in the detection-plane. The measured quantities r , c , and φ can be written as

$$r = f_r(x, y, z), \quad (2.1)$$

$$c = f_c(x, y, z), \quad (2.2)$$

$$\varphi = \Phi(x, y, z), \quad (2.3)$$

where $f_r(x, y, z)$, $f_c(x, y, z)$, and $\Phi(x, y, z)$ are system-dependent nonlinear functions. When these functions are determined through system calibrations, (x, y, z) can be found by simultaneously solving for the above nonlinear equation system. Eqs. (2.1)–(2.3) gives an abstract formulation of the profile measurement. To implement such an approach, we have to find the explicit constraints connecting the measured quantities to the unknowns.

Let us start with Eqs. (2.1) and (2.2) that signify the functionality of the imaging arm of a PSPFP system. A distorted imaging process is generally represented by the following modified projective transformation [15],

$$\begin{aligned} \frac{u + \Delta_u(u, v, w)}{w + \Delta_w(u, v, w)} &= \frac{r_{11}^{WC}x + r_{12}^{WC}y + r_{13}^{WC}z + t_1^{WC}}{r_{31}^{WC}x + r_{32}^{WC}y + r_{33}^{WC}z + t_3^{WC}}, \\ \frac{v + \Delta_v(u, v, w)}{w + \Delta_w(u, v, w)} &= \frac{r_{21}^{WC}x + r_{22}^{WC}y + r_{23}^{WC}z + t_2^{WC}}{r_{31}^{WC}x + r_{32}^{WC}y + r_{33}^{WC}z + t_3^{WC}}, \end{aligned} \quad (3)$$

where (u, v, w) denotes a distorted image point, and $\Delta_u(u, v, w)$, $\Delta_v(u, v, w)$, and $\Delta_w(u, v, w)$ are the displacements of the image point caused by distortions. Symbols ‘W’ and ‘C’ denote the world and the camera coordinate systems, respectively. (Readers should be reminded of the aforementioned convention when interpreting the meanings of r_{ij}^{WC} .)

For a fixed detection location (u_0, v_0, w_0) , the terms on the left-hand side of Eq. (3) become two constants. Simultaneously solving for these equations, we can express x and y as functions of z , as given by

$$\begin{aligned} x &= a_1z + a_0, \\ y &= b_1z + b_0, \end{aligned} \quad (4)$$

where the coefficients can be calculated through tedious but simple algebraic manipulations. Eq. (4) shows that all the points imaged to a fixed pixel lie in a straight line, usually called the line of sight of the pixel [16]. The principle rays originating from these points reach the front surface of the lens system at the same incident angle. These rays will then suffer from a series of identical refractions and will emerge from the rear surface of the lens system at the same angle. Under our definition of image points, these points produce the same image point in a fixed detection plane. Combining Eqs. (2.3) and (4) directly yields

$$\varphi = \Phi(z). \quad (5)$$

Eq. (5) indicates that, at a fixed detection location, measured phase depends only on depth position z . In a properly designed measurement system, $\Phi(z)$ is an invertible monotonic function. This allows us to represent depth z as a function of measured phase φ ,

$$z = Z(\varphi), \quad (6)$$

where $Z(\varphi)$ is the inverse function of $\Phi(z)$ which is also a monotonic function.

The proposed profile measurement scheme can now be elucidated by combining Eqs. (4) and (6) together,

$$\begin{aligned} x &= a_1z + a_0, \\ y &= b_1z + b_0, \\ z &= Z(\varphi). \end{aligned} \quad (7)$$

From Eq. (7), one can clearly find the unknown coordinates of a surface point by determining z from φ that is independent of the transverse coordinates. The latter two can be readily calculated from the first two equations in Eq. (7), once z is known. The functional form of $Z(\varphi)$ and all the coefficients involved must be found prior to the measurement through carefully designed system calibrations.

It is worth stressing that the coefficients and the functional form of $Z(\varphi)$ change with detection locations. This serves as a very efficient mechanism accounting for local distortion effects. For simplicity, the spatial dependence is omitted here but should be understood.

2.3. Phase-to-depth relation

In the following section, we focus our attention on the functional form of $Z(\varphi)$. As the first step of the analysis, we derive the ideal phase-to-depth relation under a perfect projection. Some corrective terms accounting for various distortions are then added for better accuracy of approximation.

As shown in Fig. 2, with an ideal projector, equiphase lines in the projected sinusoidal grating produce a set of equiphase planes in the image space of the projector. When the line of sight of a pixel sequentially pierces these equiphase planes, monotonically changing phase values are observed at the pixel location. For phase value φ , the corresponding depth is given by the z coordinate of the point in which the line of sight of the pixel intersects with the plane of constant phase φ .

The equations of the equiphase planes can be obtained by using the fact that they pass through the corresponding equiphase lines and the nodal point of the projection lens. For a straight line L of constant phase φ , its grating-plane expression is

$$\begin{aligned} x_G &= \frac{\varphi}{K}, \\ z_G &= 0, \end{aligned} \quad (8)$$

where K represents the wave number of the sinusoidal grating. In the projector reference system, it is represented by

$$\begin{aligned} r_{11}^{PG} x_p + r_{12}^{PG} y_p + r_{13}^{PG} z_p + t_x^{PG} &= \frac{\varphi}{K}, \\ r_{31}^{PG} x_p + r_{32}^{PG} y_p + r_{33}^{PG} z_p + t_z^{PG} &= 0. \end{aligned} \quad (9)$$

The equiphase plane produced by the projection of L is given by

$$(d_1 x_p + d_2 y_p + d_3 z_p) \varphi = e_1 x_p + e_2 y_p + e_3 z_p, \quad (10)$$

where $d_i \equiv r_{3i}^{PG} / K$ and $e_i \equiv r_{1i}^{PG} t_z^{PG} - r_{3i}^{PG} t_x^{PG}$ ($i = 1, 2, 3$).

The line of sight of the pixel can be obtained by transforming Eq. (4), which is a representation under the world coordinate system, into the projector coordinate system. This yields

$$\begin{aligned} x_p &= a'_1 z + a'_0, \\ y_p &= b'_1 z + b'_0, \\ z_p &= c_1 z + c_0. \end{aligned} \quad (11)$$

The expressions for the coefficients in Eq. (11) are omitted since they are of no interest to us. Substituting Eq. (11) into (10) gives the ideal phase-to-depth relation,

$$\bar{z} = \frac{m_1 \varphi + m_0}{n_1 \varphi + n_0}, \quad (12)$$

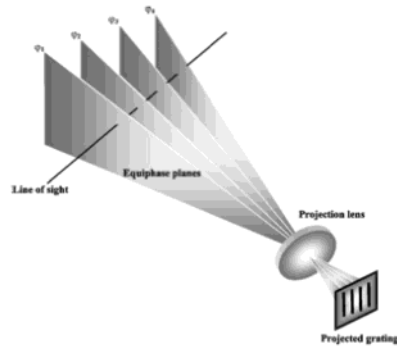


Fig. 2. Intersection of a line of sight and equiphase planes resulted from the fringe projection.

where

$$\begin{aligned} m_0 &= a'_0 e_1 + b'_0 e_2 + c_0 e_3, \\ m_1 &= -a'_0 d_1 - b'_0 d_2 - c_0 d_3, \\ n_0 &= -a'_1 e_1 - b'_1 e_2 - c_1 e_3, \\ n_1 &= a'_1 d_1 + b'_1 d_2 + c_1 d_3. \end{aligned} \quad (13)$$

In Eq. (12), \bar{z} has been used to indicate that the relationship obtained is idealized. Eq. (12) shows that $Z(\varphi)$ is nonlinear even when the projection system is free of distortions. This is a result of the divergent projection process, and is therefore inherent in non-telecentric systems. The degree of non-linearity depends on the relative magnitudes of n_1 and n_0 . A linear approximation is valid only when $n_1 \ll n_0$.

Under the influence of distortions, equiphase surfaces become slightly curved. In a plane situated at z_p , a distorted image point undergoes a transverse displacement and is related to the ideal image point by

$$\begin{aligned} x_p + \Delta_x(x_p, y_p, z_p) &= \bar{x}_p, \\ y_p + \Delta_y(x_p, y_p, z_p) &= \bar{y}_p, \end{aligned} \quad (14)$$

where $\Delta_x(x_p, y_p, z_p)$ and $\Delta_y(x_p, y_p, z_p)$ represent the displacements of the image point and the variables under the short bars are the transverse coordinates of the ideal image point. To emphasize the fact that the transverse coordinates in Eq. (10) were obtained under the perfect projection, we replace them by \bar{x}_p and \bar{y}_p , and rewrite Eq. (10) as

$$(d_1 \bar{x}_p + d_2 \bar{y}_p + d_3 z_p) \varphi = e_1 \bar{x}_p + e_2 \bar{y}_p + e_3 z_p. \quad (15)$$

Substituting Eq. (14) into (15) gives

$$[d_1(x_p + \Delta x_p) + d_2(y_p + \Delta y_p) + d_3 z_p] \varphi = e_1(x_p + \Delta x_p) + e_2(y_p + \Delta y_p) + e_3 z_p, \quad (16)$$

where $\Delta x_p \equiv \Delta_x(x_p, y_p, z_p)$ and $\Delta y_p \equiv \Delta_y(x_p, y_p, z_p)$ have been used for conciseness. As shown in Appendix A, Δx_p and Δy_p generally have the following forms,

$$\Delta x_p = \left(\sum_{0 \leq i \leq 3} k_{1i} z_p^i \right) x_p (x_p^2 + y_p^2) + \left(\sum_{0 \leq i \leq 3} s_{1i} z_p^i \right) (x_p^2 + y_p^2) + \left(\sum_{0 \leq i \leq 3} p_{1i} z_p^i \right) (3x_p^2 + y_p^2) + \left(\sum_{0 \leq i \leq 3} p_{2i} z_p^i \right) x_p y_p \quad (17)$$

and

$$\Delta y_p = \underbrace{\left(\sum_{0 \leq i \leq 3} k_{1i} z_p^i \right) y_p (x_p^2 + y_p^2)}_{\text{radial}} + \underbrace{\left(\sum_{0 \leq i \leq 3} s_{2i} z_p^i \right) (x_p^2 + y_p^2)}_{\text{thin prism}} + \underbrace{\left(\sum_{0 \leq i \leq 3} p_{2i} z_p^i \right) (3x_p^2 + y_p^2) + \left(\sum_{0 \leq i \leq 3} p_{1i} z_p^i \right) x_p y_p}_{\text{decentering}}. \quad (18)$$

Combining Eqs. (11)–(18), we get the following implicit expression for $Z(\varphi)$,

$$z = \frac{m_1 \varphi + m_0}{n_1 \varphi + n_0} + \sum_{0 \leq i \leq 6} \left(\frac{g_i - h_i \varphi}{n_1 \varphi + n_0} z^i \right). \quad (19)$$

Again, for the purpose of simplicity, the expressions for the coefficients g_i and h_i are not given. The first part of Eq. (19) can be recognized as the ideal phase-to-depth relation, while the second term originates from distortions. For well-behaved systems, the distorted image points are very close to their ideal counterparts. This enables us to substitute z with \bar{z} in the distortion term of Eq. (19). The expression resulted from such a replacement is

$$z = \frac{m_1 \varphi + m_0}{n_1 \varphi + n_0} + \sum_{0 \leq i \leq 6} \left[\frac{g_i - h_i \varphi}{n_1 \varphi + n_0} \left(\frac{m_1 \varphi + m_0}{n_1 \varphi + n_0} \right)^i \right]. \quad (20)$$

Normalizing the coefficients in Eq. (20) relative to n_0 , we can simplify it as

$$z = \frac{m'_1\varphi + m'_0}{n'_1\varphi + 1} + \sum_{0 \leq i \leq 6} \left[\frac{g_i - h_i\varphi}{n'_1\varphi + 1} \left(\frac{m'_1\varphi + m'_0}{n'_1\varphi + 1} \right) \right], \quad (21)$$

where the coefficients with a prime represent the normalized parameters. The replacement of z with \bar{z} will only cause high-order errors in the corrective term. Such small discrepancy can be partially compensated by the subsequent curve fitting process, leading to even better accuracy of approximation. There are 11 undetermined coefficients in Eq. (21), implying that at least 11 calibrations need to be taken over different depths. However, the complexity of the problem can be tailored for different system configurations. This topic will be revisited in the following section.

3. System calibrations

We are now in a position to discuss the empirical approaches for finding the parameters in the line-of-sight equation (4) and the phase-to-depth relation (21). To differentiate these two types of processing, the process of characterizing the line of sight of a pixel will be referred to as the transverse calibration, and the process of determining the parameterized $Z(\varphi)$ will be referred to as the phase-to-depth calibration.

3.1. Transverse calibration

In transverse calibration, two sinusoidal gratings with their fringes parallel to the X and the Y directions are sequentially placed in a plane situated at depth z . Assembling the images of these temporally separated but spatially overlapped gratings yields a virtual grid pattern, which serves as a metric standard in the transverse calibration. When a number of virtual grids are successively generated and measured at different depth positions, lines of sight of different pixels are traced out. Two fringes in the respective gratings are specially marked. The intersection point of these fringes in the virtual grid represents the origin of the XY plane.

Consider the center of an arbitrary pixel in which unwrapped phases φ_x and φ_y are measured when the gratings are situated at depth z . According to the assumption given in Section 2.1, the same pair of phases will be directly measured at the surface point, which is imaged to the center point. The transverse coordinates of the surface point are then given by

$$\begin{aligned} x &= \frac{\varphi_x}{K_x}, \\ y &= \frac{\varphi_y}{K_y}, \end{aligned} \quad (22)$$

where K_x and K_y are the wave numbers of the respective gratings.

Using sinusoidal gratings as calibration targets is advantageous in many aspects. By incorporating the phase-shifting detection technique into phase measurements, a high degree of accuracy is automatically achieved. Since position information is embedded in a continuous intensity distribution, every pixel can function independently in phase sampling. This results in an extremely high spatial sampling density, which is critical for measuring local distortion effects. Furthermore, when phase change is approximately linear over the detection aperture of a CCD pixel, an area sampling is equivalent to a point sampling, which takes place at the center of the pixel. In this case, detection locations are fixed as required by the proposed profile measurement scheme. When discrete patterns are employed as calibration targets, such a requirement is difficult to meet without a numerical interpolation, which is prone to various types of errors.

After measuring the virtual grids over more than two depth positions, the line of sight of each pixel is estimated by fitting measured data to a straight line. Although two coordinate measurements are sufficient

to serve this purpose, redundant measurements are highly recommended to improve the reliability of the estimation.

3.2. Phase-to-depth calibration

In the phase-to-depth calibration, a sinusoidal pattern is projected onto a flat surface perpendicular to the z direction via the projection optics. The resultant phase distribution on the flat surface is measured using the phase-shifting algorithms. The phase measurement is repeated as the flat surface is successively translated to different depth positions and stops when certain limit position is reached. The phase maps measured in this way are unwrapped first along the transversal direction and then the depth direction to recover phase continuity information. After this processing, a series of absolute phases and the associated depths are then obtained at each pixel location ready for the subsequent curve fitting.

The estimation of the distorted phase-to-depth relationship is rather complicated due to the nonlinear dependence of $Z(\varphi)$ on the coefficients involved. One needs to resort to an iterative approach for the solutions. Convergence and local minimum are always problems in this case. Things can be much simpler, however, if we estimate the ideal phase-to-depth relation and the distortion term in Eq. (21) separately.

For the ideal phase-to-depth relationship shown in the first term of Eq. (21), we can rewrite it as

$$m'_1 \varphi - n'_1 \varphi z + m'_0 = z. \quad (23)$$

By choosing φ , $z\varphi$, and 1 as the basis functions, the estimation of m'_1 , n'_1 , and m'_0 is transformed into a linear problem. When more than three pairs of phase and depth values are available for curve fitting, the least-mean-squares estimation may be used as given by

$$C = (A^T A)^{-1} A^T M, \quad (24)$$

where $C = [m'_1 \ n'_1 \ m'_0]^T$ and $M = [z_1 \ z_2 \ z_3]^T$. Matrix A , usually referred to as the design matrix, is given by

$$A = \begin{bmatrix} \varphi_1 & \varphi_1 z_1 & 1 \\ \varphi_2 & \varphi_2 z_2 & 1 \\ \varphi_3 & \varphi_3 z_3 & 1 \\ \vdots & \vdots & \vdots \\ \varphi_n & \varphi_n z_n & 1 \end{bmatrix} \quad (n \geq 3).$$

Here, superscript 'T' represents a matrix transpose and '−1' denotes a matrix inversion.

Once the ideal phase-to-depth relationship is found, we can estimate the rest of the coefficients based on the ones obtained thus far. Defining

$$\begin{aligned} \mu_i &= \frac{(m'_1 \varphi + m'_0)^i}{(n'_1 \varphi + 1)^{i+1}}, \quad 0 \leq i \leq 3, \\ v_i &= \frac{\varphi(m'_1 \varphi + m'_0)^i}{(n'_1 \varphi + 1)^{i+1}}, \quad 0 \leq i \leq 3 \end{aligned} \quad (25)$$

and

$$z_r \equiv z - \frac{m'_1 \varphi + m'_0}{n'_1 \varphi + 1}, \quad (26)$$

where z_r represents the residual depth error, we can rewrite Eq. (23) as

$$z_r = \sum_{0 \leq i \leq 6} g_i \mu_i + h_i v_i. \quad (27)$$

Again, the estimation problem is simplified as a linear one. In principle, the technique shown in Eq. (26) can be applied for estimating the coefficients when the design matrix A is properly constructed. However, this method breaks down when $A^T A$ is nearly singular. Under such circumstances, a more robust technique based on singular value decomposition can be used.

It should be mentioned that the independent variable ϕ in the parameter estimation problem at hand is not error-free, whereas the dependent variable z is usually measured at much higher accuracy and therefore can be treated as accurate. In this case, the above method does not yield the optimum estimation of the parameters in a strict sense. However, we can treat this problem as an equivalent problem with accurate ϕ but inaccurate z . It is also implied in the above method that the equivalent measurement error of z is approximately Gaussian distributed with a zero mean value.

4. Experimental results

The experiment is performed to verify the effectiveness of the proposed technique. As shown in Fig. 3, two wide-angle lenses were used for projection and imaging. It exemplifies the measurement systems with large amount of distortions. A translation stage generates motions along the depth direction during the phase-to-depth calibration. A sinusoidal fringe pattern is projected onto a flat surface, and a CCD detector obtains images on the flat surface. The resultant phase distribution on the flat surface is measured using the phase-shifting algorithms. The phase measurement is repeated as the flat is successively translated to different depths. The flat surface employed in the phase-to-depth calibration was made from a steel block. Sufficient surface diffusivity has been achieved through chemical etching processing. The depth position of both the flat surface and the gratings was monitored by a Heidenhain length gauge with accuracy of $0.1 \mu\text{m}$.

Once phase-to-depth relationship, $Z(\phi)$, at each pixel is determined, we determine the parameters in the line-of-sight equation. In the transversal calibration, two gratings with their fringes parallel to the X and the Y directions are sequentially placed in a plane situated at depth z . Assembling the images of these temporally separated but spatially overlapped gratings yields a virtual grid pattern, which serves as a metric standard in the transversal calibration. In the case of Fig. 4, the image of a grating with fringes parallel to X direction is captured by a CCD detector. When a number of virtual grids are successively generated and measured at different depth positions, lines of sight of different pixels are traced out.

Fig. 5 shows an example of the measured relation between unwrapped phase and depth at two chosen pixels. The phase-to-depth transformation for each pixel is approximated using a fifth-order polynomial fit

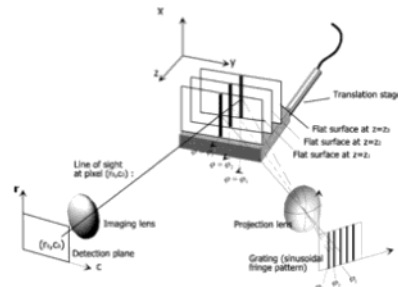


Fig. 3. Phase-to-depth calibration in a PSPFP measurement system. A sinusoidal fringe pattern is projected onto a flat surface. Its image on the flat surface is recorded from a CCD detector. In the detection plane, each pixel obtains a sequence of phase values with a sequence of the related depth positions when the translation stage generates motions along the depth direction.

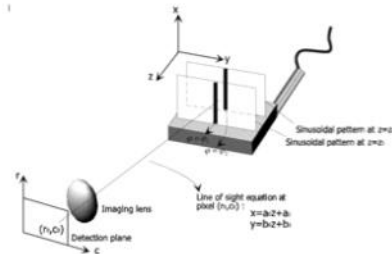


Fig. 4. Horizontal calibration in a PSPFP measurement system. The tested surface is replaced by a grating with fringes parallel to the X direction. In the detection plane, each pixel obtains two phase values from depth $z = z_1$ and $z = z_2$.

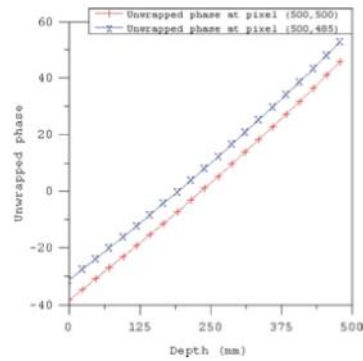


Fig. 5. Phase-to-depth correspondence measured from proposed calibration scheme. There are 21 data points measured at each pixel.

using 21 depth measurements. The measured relationship between depth and the corresponding horizontal position at two random chosen pixels is shown in Fig. 6. Again, the transformation is approximated using a fifth-order polynomial fit using 21 depth measurements.

During system calibrations, the transverse calibration and the phase-to-depth calibration were carried out in turn over a specified depth range. The calibrated volume is about 180.0 mm in width, 180.0 cm in height, and 50.0 mm in depth. Two wide-angle lenses operate at $20\times$ and $18\times$ magnification factors for projection and imaging respectively. These lenses are directed to the transverse planes of the world coordinate system at angles of $\pm 35^\circ$ for projection, and $\pm 15^\circ$ for imaging. A CCD camera with 1000×1000 pixels and a projected sinusoidal grating with a fringe period of $50 \mu\text{m}$ have been adjusted approximately conjugate to the transverse planes. No efforts have been made to enforce them to be perpendicular to the optical axes of the respective lenses.

A diffusive flat surface with a roughness of around $10 \mu\text{m}$ is employed during the phase-to-depth calibration, and a Ronchi fringe pattern with a fringe period of 2.341 mm is used for transverse calibration. Fig. 7 shows the line of sight of a typical pixel in the corner of the detection plane and the residual error after fitting the measured data to a straight line. Residual errors shown here indicate the achievable accuracy of the

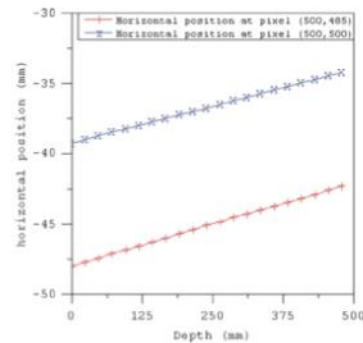


Fig. 6. Depth and horizontal position correspondence measured from transverse calibration scheme. 21 data points are measured at each pixel.

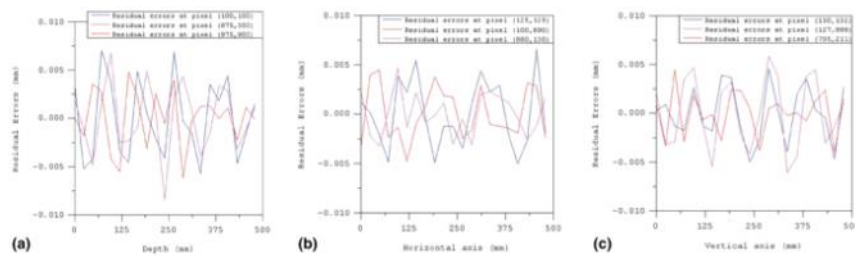


Fig. 7. Residual errors of the phase-to-depth calibration and transverse calibration. The three plots shown in each figure are the results obtained at three chosen pixel locations. Residual error is defined as the differences between measured positions and those calculated from fitting polynomials. The plots show that residual errors, which indicate the achievable accuracy of the developed calibration scheme, are approximately 10 μm .

developed phase-to-depth calibration and transverse scheme. Using this calibration scheme, a profile measurement for a fan blade was performed. Fig. 8(a) shows one perspective view of measured 3D profile of the fan blade and Fig. 8(b) shows another perspective view of measured 3D profile of the fan blade. From these two figures, it can be seen that the measured 3D profile truly reflects the 3D shape of the fan blade. To have a quantitative feeling about the proposed calibration-based phase-shifting projected fringe profilometry, a bowl shaped object with dimensions of about 160 mm in diameter and 40 mm in depth is selected as the testing object. Both the calibration-based phase-shifting projected fringe profilometry and a standard mechanical scanner (Zeiss Universal Precision Measuring Center, Model number UPMC 550) were used to measure the 3D surface profile of the bowl. Figs. 9(a) and (b) show one line of the measured 3D profile obtained from the calibration based phase-shifting projected fringe profilometry and the UPMC 550, respectively. By comparing the results from Figs. 9(a) and (b), it is found that the absolute error difference between two methods is around 5 μm . This experimental result proves that the proposed technique indeed has a very good accuracy.

The success of the calibration-based phase-shifting projected fringe profilometry is contributed by several factors. High immunity to noise and high spatial sampling density are two main factors. This

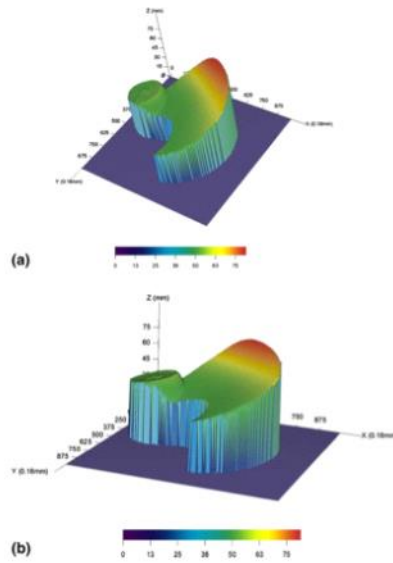


Fig. 8. Fan blade profile measured from the proposed calibration scheme.

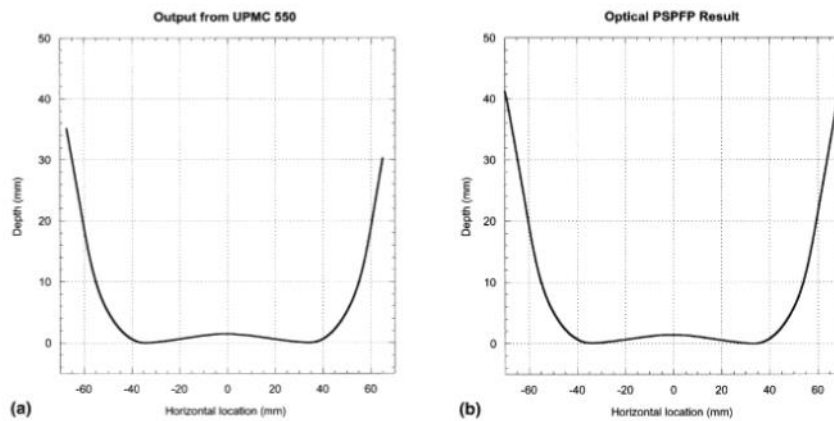


Fig. 9. A comparison between the data coming from calibration-based phase-shifting projected fringe profilometry and the conventional mechanical scanner: (a) result from phase-shifting projected fringe profilometry; (b) result from UPMC 550.

technique is capable of sampling the entire surface simultaneously with minimum requirements to the mechanical fixture. In addition to a tremendous saving in time, the benefits of using full-field detection techniques also include greatly reduced environmental vulnerability. Since profile data can be taken within a very short period of time (typically a fraction of a second), slowly varying environmental changes do not affect data acquisition significantly. In addition, fitting suitable polynomials when sufficient calibration data are measured can minimize uncertainties in phase-to-depth conversion, as well as uncertainties of depth to horizontal/vertical position conversion. In the case of our experiment, the calibration data involve 21 measurements, which are sufficient to a 5th-order polynomial fit to minimize and smooth data noise. Even though the roughness of the diffusive flat surface used for phase-to-depth calibration is 10 μm , and the overall residual errors in each direction from calibration data are also around 10 μm , we still get a very good accuracy of around 5 μm on the surface measurement of the bowl shaped object.

5. Conclusions

In conclusion, in this paper, an accurate calibration-based phase-shifting measurement technique was introduced, in which the distortion for each location was calibrated individually. The main advantages of this presented technique are: (1) since this technique uses only one-camera and one-projector configuration for calibration, it offers the advantages of higher flexibility and more compactness; (2) since it characterizes system distortions for each detection location individually, it effectively eliminates the effect of local distortion; (3) the estimation of system parameters requires only a linear optimization so that a stable numerical solution can be easily found; and (4) the calibration process covers the case in which the detection plane is not perpendicular to the optical axis of the imaging lens. By comparing the experimental data from this technique with the data from the UPMC 550, it was found that the absolute error of a bowl shaped object was around 5 μm . Thus, indeed, the presented technique has a good accuracy ($5 \mu\text{m}/180 \text{ mm} \approx 10^{-5}$), which makes it possible to have many applications to the precise engineering surface measurements such as precision gear gauge measurement and large size propeller inspection.

Acknowledgement

This work was performed under the support of the U.S. Department of Commerce, National Institute of Standards and Technology, Advanced Technology Program, Cooperative Agreement Number 70NANB7H3022. The authors are also grateful for support from the Institute for Manufacturing and Sustainment Technologies at The Pennsylvania State University's Applied Research Laboratory. The Institute is a non-profit organization sponsored by the United States Navy Manufacturing Technology (MANTECH) Program, Office of Naval Research (contract number N00014-99-0005). Any opinions, findings, conclusions or recommendations expressed in this material are those of the authors and do not necessarily reflect the views of the U.S. Navy.

Appendix A

In the following analysis, we study how distortions vary as the detection plane is translated along the optical axis of the optical system. This topic has not been fully explored in the past, although the analytical expressions for various distortions in a fixed detection plane can be found in a vast body of literature. The distortions considered include the radial distortion, the thin prism distortion, and the decentering distortion, which are responsible for most significant defects in the optical systems.

A strict ray tracing reveals that distortions change with the object position as well as the image position. For the projector in a PSPFP system, the grating plane is fixed, but the measured object may take up an extended axial range. When the axial extent of the object cannot be neglected compared with the nominal object distance, the variations of the distortions need to be taken into account in the modeling of the projection system. To show how this can be done, let us consider the radial distortion as an example.

Fig. 10 shows a plane containing an undistorted ray NP and its associated distorted ray EP' . These rays intersect with two planes situated at axial positions z_{p1} and z_{p2} forming two ideal image points P_1 and P_2 and two distorted ones P'_1 and P'_2 . Assume the radial distortion coefficients k_0 and k'_0 are known at z_{p1} and z_{p2} . Radial distortions Δr_1 and Δr_2 can then be found as

$$\Delta r_1 = k_0 r_1^3 = k_0 (z_{p1} \tan \theta)^3 \quad (\text{A.1})$$

and

$$\Delta r_2 = k'_0 r_2^3 = k'_0 (z_{p2} \tan \theta)^3. \quad (\text{A.2})$$

From the figure, it can be seen that the radial distortion at an arbitrary z_p is given by

$$\begin{aligned} \Delta r &= \left(\frac{z_{p2} - z_p}{z_{p2} - z_{p1}} \right) k_0 (z_{p1} \tan \theta)^3 + \left(\frac{z_p - z_{p1}}{z_{p2} - z_{p1}} \right) k'_0 (z_{p2} \tan \theta)^3 \\ &= \left[k_0 \left(\frac{z_{p2} - z_p}{z_{p2} - z_{p1}} \right) \left(\frac{z_{p1}}{z_p} \right)^3 + k'_0 \left(\frac{z_p - z_{p1}}{z_{p2} - z_{p1}} \right) \left(\frac{z_{p2}}{z_p} \right)^3 \right] (z_p \tan \theta)^3. \end{aligned} \quad (\text{A.3})$$

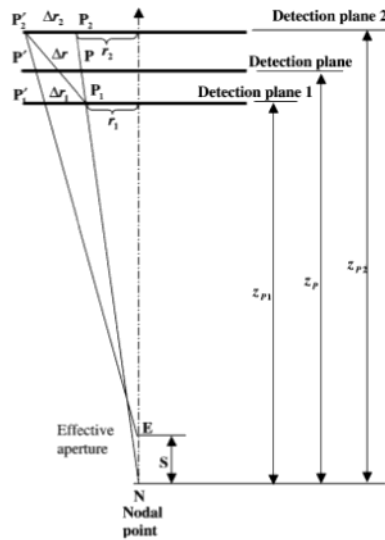


Fig. 10. Variations of the radial distortion with the depth position.

The distortion coefficient k_1 at z_p is then

$$k_1 = k_0 \left(\frac{z_{p2} - z_p}{z_{p2} - z_{p1}} \right) \left(\frac{z_{p1}}{z_p} \right)^3 + k'_0 \left(\frac{z_p - z_{p1}}{z_{p2} - z_{p1}} \right) \left(\frac{z_{p2}}{z_p} \right)^3 \quad (\text{A.4})$$

$$= \frac{\left[k_0 (z_{p1})^3 \left(\frac{z_{p2} - z_p}{z_{p2} - z_{p1}} \right) + k'_0 (z_{p2})^3 \left(\frac{z_p - z_{p1}}{z_{p2} - z_{p1}} \right) \right]}{\left(\frac{z_{p2} + z_{p1}}{2} \right)^3 \left(1 + \frac{2z_p}{z_{p2} + z_{p1}} - 1 \right)^3}. \quad (\text{A.5})$$

It is often true that the axial extent of the test object is much smaller than the average object distance,

$$(z_{p2} - z_{p1}) \ll \frac{z_{p2} + z_{p1}}{2}.$$

Expanding the denominator of Eq. (A.5) into Taylor series and keeping up to the second-order power, we can express k_1 as

$$k_1 = \left(\frac{z_{p2} + z_{p1}}{2} \right)^{-3} \left[k_0 z_{p1}^3 \left(\frac{z_{p2} - z_p}{z_{p2} - z_{p1}} \right) + k'_0 z_{p2}^3 \left(\frac{z_p - z_{p1}}{z_{p2} - z_{p1}} \right) \right] \times \left[1 - 3 \left(\frac{2z_p}{z_{p2} + z_{p1}} - 1 \right) + 6 \left(\frac{2z_p}{z_{p2} + z_{p1}} - 1 \right)^2 \right]. \quad (\text{A.6})$$

Eq. (A.6) has the following general form,

$$k_1 = \sum_{i=0}^3 k_{1i} z_p^i. \quad (\text{A.7})$$

Decomposing the radial distortion into its transverse components, we have

$$\Delta x'_p = \left(\sum_{0 \leq i \leq 3} k_{1i} z_p^i \right) x_p (x_p^2 + y_p^2) \quad (\text{A.8})$$

and

$$\Delta y'_p = \left(\sum_{0 \leq i \leq 3} k_{1i} z_p^i \right) y_p (x_p^2 + y_p^2). \quad (\text{A.9})$$

The decentering and the thin prism distortions can be analyzed in a rather similar way. In both cases, the ideal and the distorted rays are no longer coplanar because of the nonzero tangential distortions. However, an analysis similar to the above one can still be applied to each of the transverse components of these distortions. Accordingly, NP and EP' should be thought as the projections of the ideal and the distorted rays in the XZ or the YZ planes. Following the procedure outlined, we can get the following expressions for the distortions varying in the axial directions,

$$\Delta x''_p = \left(\sum_{0 \leq i \leq 3} s_{1i} z_p^i \right) (x_p^2 + y_p^2), \quad (\text{A.10})$$

$$\Delta y''_p = \left(\sum_{0 \leq i \leq 3} s_{2i} z_p^i \right) (x_p^2 + y_p^2)$$

for the thin prism distortion, and

$$\begin{aligned}\Delta x_p^m &= \left(\sum_{0 \leq i \leq 3} p_{1i} z_p^i \right) (3x_p^2 + y_p^2) + \left(\sum_{0 \leq i \leq 3} p_{2i} z_p^i \right) x_p y_p, \\ \Delta y_p^m &= \left(\sum_{0 \leq i \leq 3} p_{2i} z_p^i \right) (3x_p^2 + y_p^2) + \left(\sum_{0 \leq i \leq 3} p_{1i} z_p^i \right) x_p y_p\end{aligned}\quad (\text{A.11})$$

for the decentering distortion. The transverse components of the total distortion are

$$\begin{aligned}\Delta x_p &= \left(\sum_{0 \leq i \leq 3} k_{1i} z_p^i \right) x_p (x_p^2 + y_p^2) + \left(\sum_{0 \leq i \leq 3} s_{1i} z_p^i \right) (x_p^2 + y_p^2) + \left(\sum_{0 \leq i \leq 3} p_{1i} z_p^i \right) (3x_p^2 + y_p^2) \\ &\quad + \left(\sum_{0 \leq i \leq 3} p_{2i} z_p^i \right) x_p y_p\end{aligned}\quad (\text{A.12})$$

and

$$\Delta y_p = \underbrace{\left(\sum_{0 \leq i \leq 3} k_{1i} z_p^i \right) y_p (x_p^2 + y_p^2)}_{\text{radial}} + \underbrace{\left(\sum_{0 \leq i \leq 3} s_{2i} z_p^i \right) (x_p^2 + y_p^2)}_{\text{thin prism}} + \underbrace{\left(\sum_{0 \leq i \leq 3} p_{2i} z_p^i \right) (3x_p^2 + y_p^2) + \left(\sum_{0 \leq i \leq 3} p_{1i} z_p^i \right) x_p y_p}_{\text{decentering}},\quad (\text{A.13})$$

It should be mentioned that Abdel-Aziz and Karara [17] has used a similar method to discuss the dependence of the radial distortion on the object distance. However, our analysis is carried out under the generalized definition of image points given in Section 2.1 and its conclusions can be applied to the transverse components of all three major distortions.

References

- [1] H. Takasaki, *Appl. Opt.* 9 (1970) 1467.
- [2] V. Srinivasan, H.C. Liu, M. Halioua, *Appl. Opt.* 24 (2) (1985) 185.
- [3] T. Matsumoto, Y. Kitagawa, T. Minemoto, *Opt. Eng.* 35 (1996) 1754.
- [4] G. Lu, S. Wu, N. Palmer, H. Liu, *Proc. SPIE* 3520 (1998) 52.
- [5] G. Wiora, *Proc. SPIE* 4117 (2000) 289.
- [6] C. Zhang, P.S. Huang, F.P. Chiang, *Proc. SPIE* 4189 (2000) 122.
- [7] Z.W. Zhong, C.P. Han, A.K. Asundi, *Proc. SPIE* 4398 (2001) 182.
- [8] K. Creath, in: E. Wolf (Ed.), *Progress in Optics*, vol. 26, North-Holland, Amsterdam, 1988, p. 350.
- [9] C.S. Vikram, *Optik (Jena)* 111 (12) (2000) 563.
- [10] F. Chen, G.M. Brown, M. Song, *Opt. Eng.* 39 (2000) 10.
- [11] O.D. Faugeras, G. Toscani, in: *Proc. Int. Conf. Comput. Vision. Patt. Recogn.* (Miami Beach, FL), Aug. 1983, p. 996.
- [12] A. Isaguirre, P. Pu, J. Summers, in: *Proc. IEEE Int. Conf. Robotics Automat.* (St. Louis), 1985, p. 74.
- [13] J. Weng, P. Cohen, M. Herniou, *IEEE Trans. PAMI* 14 (1992) 965.
- [14] K.D. Gremban, C.E. Thorpe, T. Kande, in: *IEEE Robotics Automat. Proceedings. International Conference* (Philadelphia, PA), 1988, p. 947.
- [15] W. Faig, *Photogramm. Eng. Remote Sensing* 41 (12) (1975) 1479.
- [16] H.A. Martins, J.R. Birk, R.B. Kelley, *Comput. Graphics Image Process.* 17 (1981) 173.
- [17] Y.I. Abdel-Aziz, H.M. Karara, in: *Symposium on Close-Range Photogrammetry* (Urbana, IL) Jan. 1971, p. 1.